Novel Interparticle Spatial Properties of Hydrogen-Bonding Mediated Nanoparticle Assembly

Li Han, Jin Luo, Nancy N. Kariuki, Mathew M. Maye, Vivian W. Jones,† and Chuan Jian Zhong*

Department of Chemistry, State University of New York at Binghamton, Binghamton, New York 13902

Received August 1, 2002. Revised Manuscript Received September 26, 2002

Results of an investigation of hydrogen-bonding mediated interparticle assembling and spatial properties from extremely dilute concentrations of the mediation agent are reported. Nanoparticles consisting of highly monodispersed decanethiolate-capped gold nanocrystal cores and α,ω-mercapto-alkanoic acids are highlighted as a model system. The formation of a stable ordered array is demonstrated via manipulating the constituents in solution. Infrared reflection spectroscopy, spectrophotometry, transmission electron microscopy, and atomic force microscopy have been utilized to probe the interparticle structural and spatial properties. A "squeezed" interparticle spatial model involving both hydrogen-bonding at the carboxylic acid groups and cohesive van der Waals interaction through interdigitation of the capping decanethiolate molecules is concluded to be responsible for the interparticle assembling forces. This interparticle spatial property depends on the relative amount of the hydrogen-bonding mediation agent, nanocrystal core size, and size monodispersity. Implications of these findings to the creation of well-defined nanostructures from nanoscale building blocks toward functional nanomaterials are also discussed.

Introduction

The importance of understanding factors governing the creation of nanoparticle assembly stems from the desire to precisely manipulate nanostructured functional properties for optical, microelectronic, magnetic, catalytic, and chemical/biological applications.[1,2] The desire is recently highlighted by attributes of engineering metallic or semiconductor nanoparticles as building blocks in terms of size monodispersity, core−shell processibility, solubility, stability, self-assembly capability, and interfacial reactivities. Nanoparticles and assemblies toward macroscopic materials of both fundamental and technological interests have been reported, including two-phase synthesis of monolayer-protected nanoparticles,[3−5] stepwise layer-by-layer construction,[5−8] and DNA and other molecular assembling strategies.[9−12] Although there is a wide range of interests in exploring these nanostructured applications, the lack of knowledge of interparticle structure−reactivity correlation limits our ability to precisely control nanoparticle

* To whom correspondence should be addressed. Phone: 607-777-4605. E-mail: cjzhong@binghamton.edu.

† 3M Corporate Analytical Technology Center, 3M Center, St. Paul, MN 55144-1000.

(1) (a) Templeton, A. C.; Wuelfing, W. P.; Murray, R. W. *Acc. Chem. Res.* **2000**, *33*, 27. (b) Shipway, A. N.; Katz, E.; Willner, I. *ChemPhysChem* **2000**, *1*, 18. (c) Storhoff, J. J.; Mirkin, C. A. *Chem. Rev.* **1999**, *99*, 1849.

(2) (a) Zhong, C. J.; Maye, M. M. *Adv. Mater.* **2001**, *13*, 1507. (b) Han, L.; Daniel, D. R.; Maye, M. M.; Zhong, C. J. *Anal. Chem.* **2001**, *73*, 4441.

(3) (a) Brust, M.; Walker, M.; Bethell, D.; Schiffrin, D. J.; Whyman, R. *J. Chem. Soc., Chem. Commun.* **1994**, 801. (b) Gittins, D. I.; Bethell, D.; Schiffrin D. J.; Nichols, R. J. *Nature* **2000**, *408*, 67.

(4) (a) Hostetler, M. J.; Wingate, J. E.; Zhong, C. J.; Harris, J. E.; Vachet, R. W.; Clark, M. R.; Londono, J. D.; Green, S. J.; Stokes, J. J.; Wignall, G. D.; Glish, G. L.; Porter, M. D.; Evans, N. D.; Murray, R. W. *Langmuir* **1998**, *14*, 17. (b) Zamborini, F. P.; Gross, S. M.; Murray, R. W. *Langmuir* **2001**, *17*, 481.

(5) (a) Wang, Z. L. *Adv. Mater.* **1998**, *10*, 13. (b) Whetten, R. L.; Khoury, J. T.; Alvarez, M. M.; Murthy, S.; Vezmar, I.; Wang, Z. L.; Stephens, P. W.; Cleveland, C. L.; Luedtke, W. D.; Landman, U. *Adv. Mater.* **1996**, *8*, 428. (c) Wang, Z. L.; Harfenist, S. A.; Vezmar, I.; Whetten, R. L.; Bentley, I.; Evans, N. D.; Alexander, K. B. *Adv. Mater.* **1998**, *10*, 808.

(6) (a) Brust, M.; Bethell, D.; Kiely, C. J.; Schiffrin, D. J. *Langmuir* **1998**, *14*, 5425. (b) Bethell, D.; Brust, M.; Schiffrin D. J.; Kiely, C. *J. Electroanal. Chem.* **1996**, *409*, 137. (c) Brust, M.; Kiely, C. J.; Bethell, D.; Schiffrin, D. J. *J. Am. Chem. Soc.* **1998**, *120*, 12367. (d) Baum, T.; Bethell, D.; Brust, M.; Schiffrin, D. J. *Langmuir* **1985**, *15*, 866.

(7) (a) Musick, M. D.; Pena, D. J.; Botsko, S. L.; McEvoy, T. M.; Richardson, J. N.; Natan, M. J. *Langmuir* **1999**, *15*, 844. (b) Keating, C. D.; Musick, M. D.; Lyon, L. A.; Brown, K. R.; Baker, B. E.; Pena, D. J.; Feldheim, D. L.; Mallouk, T. E.; Natan, M. J. *ACS Symp. Ser.* **1997**, *679*, 7.

(8) (a) Zamborini, F. P.; Hicks, J. F.; Murray, R. W. *J. Am. Chem. Soc.* **2000**, *122*, 4514. (b) Templeton, A. C.; Zamborini, F. P.; Wuelfing, W. P.; Murray, R. W. *Langmuir* **2000**, *16*, 6682. (c) Wuelfing, W. P.; Zamborini, F. P.; Templeton, A. C.; Wen, X. G.; Yoon, H.; Murray, R. W. *Chem. Mater.* **2001**, *13*, 87.

(9) (a) Mirkin, C. A.; Letsinger, R. L.; Mucic, R. C.; Storhoff, J. J. *Nature* **1996**, *382*, 607. (b) Elghanian, R.; Storhoff, J. J.; Mucic, R. C.; Letsinger, R. L.; Mirkin, C. A. *Science* **1997**, *277*, 1078. (c) Taton, T. A.; Mucic, R. C.; Mirkin, C. A.; Letsinger, R. L. *J. Am. Chem. Soc.* **2000**, *122*, 6305−6306. (d) Storhoff, J. J.; Lazarides, A. A.; Mucic, R. C.; Mirkin, C. A.; Letsinger, R. L.; Schatz, G. C. *J. Am. Chem. Soc.* **2000**, *122*, 4640−4650.

(10) (c) Bruchez, M.; Moronne, M.; Gin, P.; Weiss, S.; Alivisatos, A. P. *Science* **1998**, *281*, 2013. (d) Alivisatos, A. P.; Johnsson, K. P.; Peng, X. G.; Wilson, T. E.; Loweth, C. J.; Bruchez, M. P.; Schultz, P. G. *Nature* **1996**, *382*, 609.

(11) Mbindyo, J. K. N.; Reiss, B. D.; Martin, B. R.; Keating, C. D.; Natan, M. J.; Mallouk, T. E. *Adv. Mater.* **2001**, *13*, 249.

(12) (a) Boal, A. K.; Rotello V. M. *J. Am. Chem. Soc.* **1999**, *121*, 4914. (b) Liu, J.; Mendoza, S.; Roman, E.; Lynn, M. J.; Xu, R. L.; Kaifer, A. E. *J. Am. Chem. Soc.* **1999**, *121*, 4304. (c) Lahav, M.; Shipway, A. N.; Willner, I. *J. Chem. Soc., Perkin Trans.* **1999**, *2*, 1925. (d) Chen, S. W.; Pei, R. J. *J. Am. Chem. Soc.* **2001**, *123*, 10607. (e) Kim, B.; Tripp, S. L.; Wei, A. *J. Am. Chem. Soc.* **2001**, *123*, 7955. (f) Han, L.; Daniel, D. R.; Maye, M. M.; Zhong, C. J. *Anal. Chem.* **2001**, *73*, 4441.

10.1021/cm0208051 CCC: $25.00
Published on Web 11/28/2002

Scheme 1. Two Extremes of 2D Interparticle Assembly of Nanoparticles toward a Domain Size of Radius R: Dense Packing (a) and Branching Growth (b)

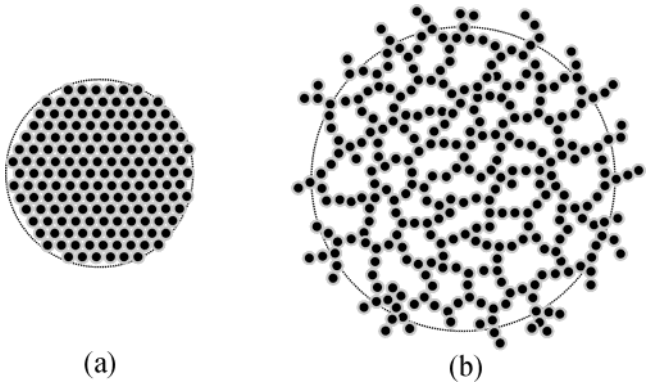

organization, ordering, and other morphological properties.

This paper reports novel findings of a study of hydrogen-bonding mediated interparticle assembly from core−shell nanoparticles consisting of nanocrystal core and organic monolayer shell, e.g., alkanethiolate-capped gold nanoparticles. In comparison with covalent, electrostatic, or van der Waals (VW) interactions, hydrogen-bonding has an intermediate binding strength and binding reversibility, which offers a flexible and controllable pathway for structural manipulation and correlation. Some of the attributes have been demonstrated in several recent reports for supramolecular and nanoparticle assemblies.[12−15] In the hydrogen-bonding mediated pathway, we consider two extremes of a hypothesis of the nanoparticle assembly (Scheme 1): (a) a dense packing and (b) a 2D fractal growth of the linked particles. The interparticle properties are dependent on the core−shell size and the actual degree of packing or branching. Pore diameters or densities up to $\sim 10^{12}$ pores/cm^2 for a layer of 5-nm sized particles could be estimated. Although VW force is one of the most common intermolecular or interparticle forces responsible for the formation of ordered arrays in evaporated nanoparticles,[5] particles held together by such a nonspecific force are, however, not fully controllable or chemically or mechanically stable on macroscopic materials scale. In contrast, chemically specific binding (e.g., covalent or H-bonding) could overcome the weakness, though observations of large domains of highly ordered organization are very limited.[16] We rationalized that it is possible to use a combination of these two forces for constructing nanoparticle assembly by manipulating the chemically specific constituent. For example, if the relative molar ratio of the hydrogen-bonding ligand (R_2) vs methyl-terminated alkyl capping molecules (R_1) ($\propto$ moles of R_1-capped nanoparticles (NP)), i.e., N_L/N_{NP}, is manipulated, the interparticle interaction in the assembly could consist of a balance of hydrogen-bonding and VW forces, leading to the regulation of the interparticle packing or spatial properties.

We show herein that the intermolecular hydrogen-bonding mediation of gold nanoparticle assembly by carboxylic acid groups and the hydrophobic interaction of alkanethiolates constitute an excellent model system for exploring the above hypothesis. We demonstrate that a very small fraction of the hydrogen-bonding agent is sufficient for mediating the assembly toward chemically stable and ordered array morphologies. In view of the diversity of place-exchange reactivities of monolayer-capped nanoparticles[17] and the importance of hydrogen-bonding in materials and biological or biomimetic systems,[15a] an in-depth understanding of the interparticle spatial properties of the hydrogen-bonding mediated nanoparticle assembly could also facilitate the design of nanostructures for mimicking biological or synthetic receptors,[12,18] and a wide range of applications such as filtration, sensing, and catalysis.[2]

Experimental Section

Chemicals. Decanethiol (DT, 96%), hydrogen tetrachloroaurate ($HAuCl_4$, 99%), tetraoctylammonium bromide (TOABr, 99%), 11-mercaptoundecanoic acid (MUA, 95%), 16-mercaptohexadecanoic acid (MHA, 90%), and 1,9-nonanedithiol (NDT, 95%) were purchased from Aldrich and used as received. Other chemicals included hexane (99.9%) and toluene (99.8%) from Fisher, and ethanol (99.9%) from Aldrich. Water was purified with a Millipore Milli-Q water system.

Synthesis. Gold nanoparticles of 2 nm core size encapsulated with DT monolayer shells were synthesized according to Schiffrin's two-phase method[3] and synthetic modifications.[4] Details for the synthesis of our 2-nm gold nanoparticles (Au_{2-nm}, 1.9 ± 0.7 nm) were recently described.[19] Gold nanoparticles of larger sizes were produced from Au_{2-nm} particles by a thermally activated processing route recently developed in our laboratory.[19] In this route, the core−shell structure undergoes desorption/re-deposition and coalescence/growth, and evolves toward a larger core size. In addition to nanoparticles of the core size of 5.2 ± 0.3 nm (Au_{5-nm}),[19] we were also able to process the nanoparticles toward different core sizes of high monodispersity. In this work, we largely focus on the ~6-nm gold nanoparticles produced from the same procedure, but by controlling a slightly higher evolution temperature (~146 °C) and using longer annealing time at 100 °C (4 h). The TEM micrograph for the processed particles is shown in Figure 1, along with the size distribution histogram. This sample was prepared by evaporation of a drop of hexane

(13) Boal, A. K.; Rotello, V. M. *Langmuir* **2000**, *16*, 9527.
(14) (a) Kim, Y. J.; Johnson, R. C.; Hupp, J. T. *Nano Lett.* **2001**, *1*, 165. (b) Weisbecker, C. S.; Merritt, M. V.; Whitesides, G. M. *Langmuir* **1996**, *12*, 3763. (c) Johnson, S. R.; Evans, S. D.; Brydson, R. *Langmuir* **1998**, *14*, 6639. (d) Mayya, K. S.; Patil, V.; Sastry, M. *Langmuir* **1997**, *13*, 3944. (e) Hao, E.; Lian, T. *Chem. Mater.* **2000**, *12*, 3392.
(15) (a) Zheng, W. X.; Maye, M. M.; Leibowitz, F. L.; Zhong, C. J. *Anal. Chem.* **2000**, *72*, 2190. (b) Han, L.; Maye, M. M.; Leibowitz, F. L.; Ly, N. K.; Zhong, C. J. *J. Mater. Chem.* **2001**, *11*, 1259. (c) Leibowitz, F. L.; Zheng, W. X.; Maye, M. M.; Zhong, C. J. *Anal. Chem.* **1999**, *71*, 5076.
(16) Andres, R. P.; Bielefeld, J. D.; Henderson, J. I.; Janes, D. B.; Kolagunta, V. R.; Kubiak, C. P.; Mahoney, W. J.; Osifchin, R. G. *Science* **1996**, *273*, 1690.
(17) (a) Hostetler, M. J.; Green, S. J.; Stokes, J. J.; Murray, R. W. *J. Am. Chem. Soc.* **1996**, *118*, 4212. (b) Ingram, R. S.; Hostetler, M. J.; Murray, R. W. *J. Am. Chem. Soc.* **1997**, *119*, 9175. (c) Hostetler, M. J.; Templeton, A. C.; Murray, R. W. *Langmuir* **1999**, *15*, 3782. (d) Templeton, A. C.; Hostetler, M. J.; Kraft, C. T.; Murray, R. W. *J. Am. Chem. Soc.* **1998**, *120*, 1906. (e) Templeton, A. C.; Hostetler, M. J.; Warmoth, E. K.; Chen, S. W.; Hartshorn, C. M.; Krishnamurthy, V. M.; Forbes, M. D. E.; Murray, R. W. *J. Am. Chem. Soc.* **1998**, *120*, 4845. (f) Wuelfing, W. P.; Templeton, A. C.; Hicks, J. F.; Murray, R. W. *Anal. Chem.* **1999**, *71*, 4069. (g) Chen, S. W.; Murray, R. W. *J. Phys. Chem. B* **1999**, *103*, 9996. (h) Templeton, A. C.; Cliffel, D. E.; Murray, R. W. *J. Am. Chem. Soc.* **1999**, *121*, 7081.
(18) (a) Mallouk, T. E.; Gavin, J. A. *Acc. Chem. Res.* **1998**, *31*, 209. (b) Fuhrhop, J−H., Ed.; *Membranes and Molecular Assemblies: The Synkinetic Approach*; Royal Society of Chemistry: Cambridge, 1994; p 149.
(19) (a) Maye, M. M.; Zheng, W. X.; Leibowitz, F. L.; Ly, N. K.; Zhong, C. J. *Langmuir* **2000**, *16*, 490. (b) Maye, M. M.; Zhong, C. J. *J. Mater. Chem.* **2000**, *10*, 1895.

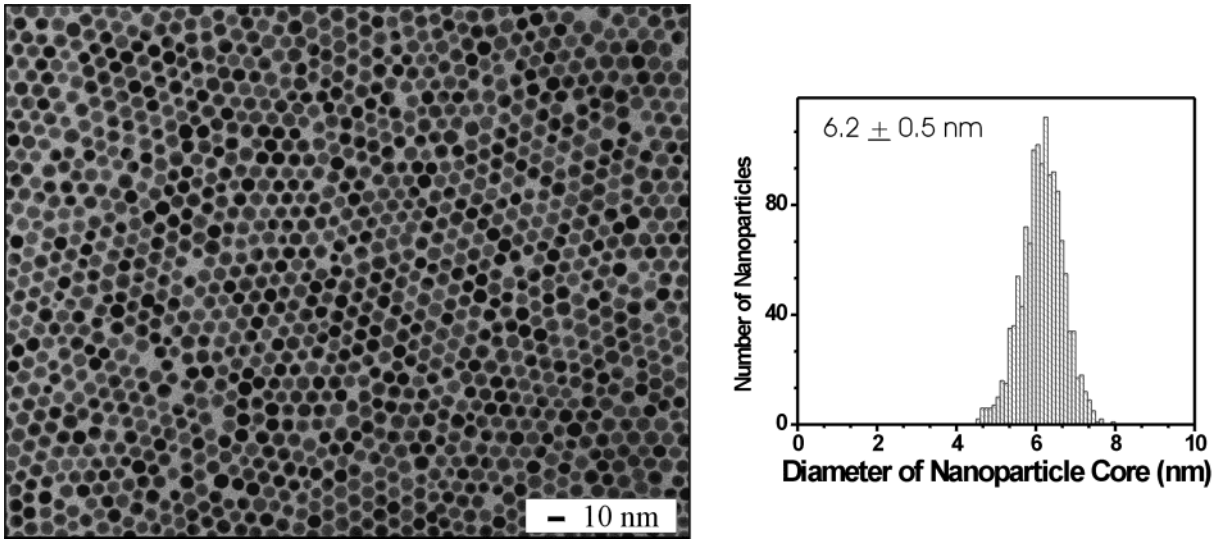

Figure 1. TEM micrograph and size distribution histogram (based on 1300 counts) of DT-capped Au nanoparticles produced by the thermally activated processing route.

solution of DT/Au_{6-nm} (~0.24 μM) on a carbon-coated Cu grid. We note that the difference between darker and lighter appearance of the particles is likely due to the presence of slightly different crystallite orientations.[5c] These particles have an average diameter of 6.2 nm with a small standard deviation of ±0.5 nm (Au_{6-nm}).

Preparation. The nanoparticle assembling process involved immersing an appropriate substrate in a hexane solution of the gold nanoparticles and the mediator agents. This procedure is largely the same as that recently reported for assembling nanoparticles of 2~5 nm core sizes[15] except for a key difference in concentrations of the constituents. In the previous procedure, concentrations of the 5-nm nanoparticles and MUA were relatively high, typically in 1.0 μM for Au_{5-nm}, and 0.05 mM for MUA (the molar ratio of MUA to Au_{5-nm} was ≥50). In the present work, concentrations of the Au_{6-nm} and MUA or MHA ligands were much more dilute, typically 0.2~1.0 μM Au_{6-nm} and 0.3~1.5 μM MUA or MHA. The relative molar ratio of the carboxylic acid ligand (L) vs the methyl-capped nanoparticles (NP), i.e., N_L/N_{NP}, is controlled in the preparation procedure. We focused primarily on molar ratios close to ~1. The nanoparticle concentrations were determined by spectrophotometric calibration, which was based on a truncated octahedron model for the particle shape.[4a]

Substrates used for the thin film preparation included glass, gold-film-coated mica, and carbon-film-coated TEM grid. The general preparation involves immersion of substrates, glass, or gold film on glass, into a solution of nanoparticles and cross-linking agents at room temperature. The film preparation involved addition of the linker solution to the nanoparticle solution followed by a quick mixing. The freshness of the solution was thus about a few seconds. The film formation immediately follows the exchange reaction, as known from the previous exponential growth kinetics.[15] Under the experimental condition of this paper, the thin film formation could be detected in as less as 5 min. The substrates were immersed vertically to ensure that the film was free of powder deposition. At a controlled immersion time, the film-deposited substrates were emersed and immediately rinsed thoroughly with the solvent. The thin film was dried under nitrogen or air before characterizations.

Instrumentation and Measurements. UV−Visible (UV−Vis) spectra were acquired with a HP 8453 spectrophotometer. Nanoparticle samples were dissolved in hexane. Thin film samples were deposited on glass substrates. The spectra were collected over the range of 200−1100 nm.

Infrared reflectance spectra (IRS) were acquired with a Nicolet 760 ESP FT-IR spectrometer that was purged with boil-off from liquid N_2. The spectrometer was equipped with a liquid-nitrogen-cooled HgCdTe detector, and the measurements were performed in an external reflection mode using *p*-polarized light at an incident angle of 82°. An octadecanethiolate-d_{37} monolayer on gold was used as the reference. Gold thin film on Cr-primed glass (Au/glass) was used as a substrate for the IRS measurement. The spectral deconvolution was based on the convergence of a Marquardt−Levenberg algorithm to values that gave the best least-squares fit to the spectral data using a Lorentzian-type band shape.

Transmission electron microscopy (TEM) was performed on a Hitachi H-7000 electron microscope (100 kV). The nanoparticle samples dissolved in hexane or toluene solution were drop-cast onto a carbon-coated copper grid sample holder followed by solvent evaporation in air at room temperature.

A Multimode NanoScope IIIa (Digital Instruments) was utilized for imaging. The TappingMode (TM)-AFM was used for imaging. Standard silicon cantilevers (Nanoprobes) were used. The instrument was calibrated by imaging standard grating samples.

Quartz crystal microbalance (QCM) measurement was carried out using an oscillation circuit (oscillator MC12061L, Newark Electronics) with a HP frequency counter (5302A). Gold films were deposited onto AT-cut and polished quartz crystals with a 9 MHz fundamental resonance frequency.

Results and Discussion

1. Interparticle Structure. *A. UV−Vis Charactrization.* Our initial examination of the film solubility indicated that the thin film assembled from a hexane solution of DT/Au_{5-nm} (1.0 μM) and MUA (0.06 mM) was not soluble in either nonpolar solvent (e.g., hexane) or polar solvent (e.g., ethanol). The blue color of the thin film remained intact for months. Although the insolubility in nonpolar solvent was expected, the insolubility in polar ethanol solvent was initially a surprise. As will be further evidenced in the structural characterizations, the film is hydrophobic due to a relatively low extent of exchange of DT by MUA from the low molar ratios (1~100) of MUA vs DT/Au_{5-nm} particles used in the assembling solution. This was further supported by the fact that a large excess of MUA (~90 mM) must be added into the ethanol solution in order for the thin film assembly to become completely soluble in the solvent. Evidently, a further exchange between the excess MUA in the solution and the remaining DT molecules on the nanocrystals occurs, leading to the eventual dissolution

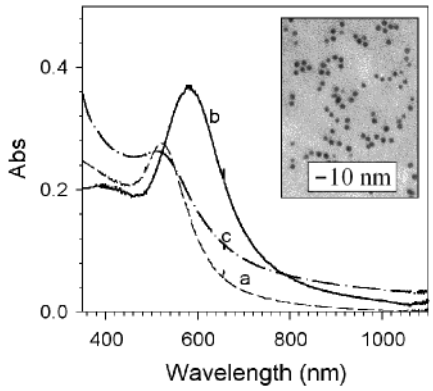

Figure 2. UV−Vis spectra: (a) DT/Au_{6-nm} in hexane; (b) MUA-Au_{6-nm} film on glass substrate; and (c) the MUA-Au_{6-nm} film dissolved in an ethanolic solution of 90 mM MUA. Inset: TEM image of the nanoparticles sampled from the dissolved solution.

and the reappearance of the original color of gold nanoparticles in solution.

As a further confirmation of the individual nanoparticle integrity, the nanoparticles dissolved in the presence of excess MUA were characterized using UV−Vis spectrophotometry. Figure 2 shows a typical set of spectra comparing the SP band characteristics for the starting DT-capped Au_{5-nm} nanoparticles in hexane (a), the MUA-linked Au_{5-nm} film on a glass slide (b), and the particles produced from dissolution of the film in an ethanolic solution of MUA (90 mM) (c). It is evident that the SP band for the nanoparticles dissolved basically returned in wavelength from 580 nm for the assembled film to 520 nm that is characteristic of the Au_{5-nm} in the solution. A similar result was also observed for Au_{6-nm}. The shift of the SP band from solution to film reflects changes in the interparticle distance and the dielectric medium.[15a,20] The subtle difference in peak shape between the initial and the redissolved nanoparticles is due to differences in solvent, capping agent, and concentration.[20] A TEM examination of the nanoparticles sampled from the dissolved nanoparticle solution (Figure 2 insert) clearly supports the UV−Vis data, conforming that the redissolved nanoparticle cores remain the same as the starting nanoparticles in terms of size. The assembling and disassembling processes do not change the size of the original nanocrystals.

Our results indicate that the solubility of the MUA-linked films is dependent on the nanocrystal core size and the surface concentration of CO_2H groups in the shell. In contrast to the poor solubility for the MUA-linked Au_{5-nm} or Au_{6-nm} film, the MUA-linked Au_{2-nm} film was found to be completely soluble in an ethanol solvent even in the absence of MUA. In this case, the solubility involved a combination of the low-molecular-mass effect and the more extensive exchange of MUA at the small sized particles. A NMR study of the extent of exchange revealed ~8% for Au_{5-nm} particles prepared from a much higher MUA-to-Au_{5-nm} ratio (50), and ~46% for Au_{2-nm} particles prepared from a much higher MUA-to-Au_{2-nm} ratio (200);[21] the latter is in a close agreement with a recent report for similar systems under a different preparative condition.[22] The MUA-linked Au_{6-nm} film from the dilute MUA concentrations must have a much lower extent of exchange, which is addressed next by IRS characterization.

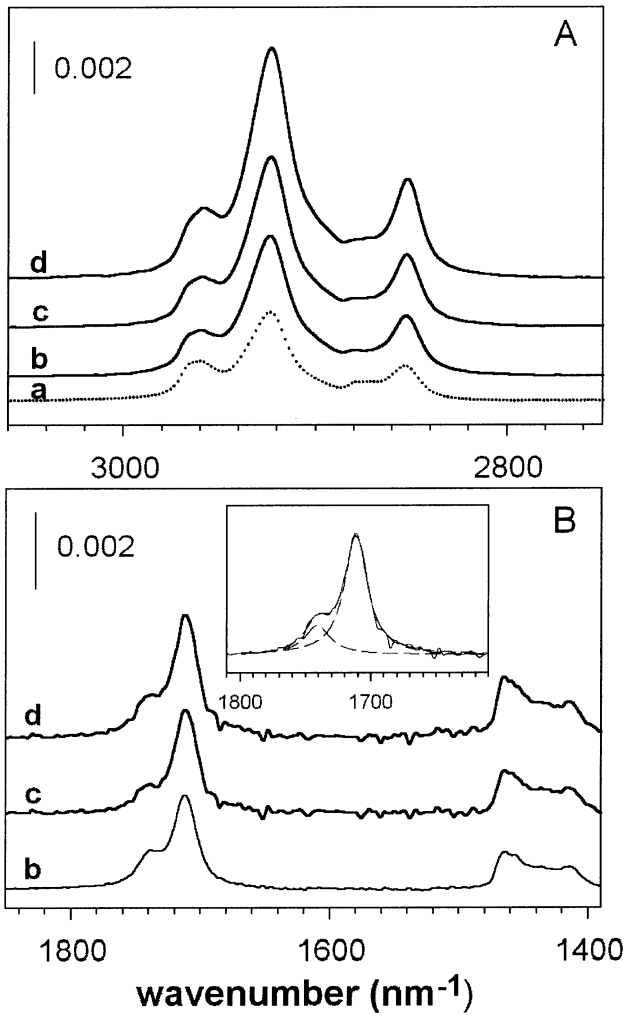

Figure 3. IRS spectra in high (A) and low (B) frequency regions for MUA-linked Au_{6-nm} films assembled from a hexane solution of [Au_{6-nm}] = 0.48 μM and [MUA] = 3.0 μM as a function of assembling time ($t_{assembly}$: 15 (b), 30 (c), and 120 (d) min). Dotted line (a): DT/Au_{6-nm} cast on Au film/glass substrate. Insert: spectral deconvolution of the carbonyl-stretching envelope.

B. IRS Characterization. To probe the structural properties, we carefully examined the IRS spectral evolution of the thin film assembly as a function of assembling time from the dilute solution, focusing on the nanoparticle assembly formed at the initial stage. Figure 3 shows a typical set of IRS spectra in both high (A) and low (B) frequency regions for samples prepared at a relatively low MUA concentration (3.0 μM). The MUA-to-Au_{6-nm} molar ratio is ~6. The spectrum for DT-capped gold nanoparticles prepared by casting on a gold film substrate is included for comparison (dashed line). The diagnostic bands include carbonyl stretching modes ($\nu_{C=O}$) in the low-frequency region and methyl and

(20) (a) Alvarez, M. M.; Khoury, J. T.; Schaaff, T. G.; Shafigullin, M. N.; Vezmar, I.; Whetten, R. L. *J. Phys. Chem.* B **1997**, *101*, 3706. (b) Link, S.; El-Sayed, M. A.; *Int. Rev. Phys. Chem.* **2000**, *19*, 409.

(21) Kariuki, N.; Han, L.; Ly, N. K.; Peterson, M. J.; Maye, M. M.; Liu, G.; Zhong, C. J. *Langmuir* **2002**, *18*, 8255.

(22) Hicks, J. F.; Seok-Shon Y.; Murray, R. W. *Langmuir* **2002**, *18*, 2288.

Table 1. Relative Ratio of the Peak Areas Based on Spectral Deconvolution of the Spectra in the C−H Stretching and the Carbonyl Stretching Regions

	IRS peak area ratio	
assembling time (min)	A[$\nu_a(CH_3)$]/ A[$\nu_a(CH_2)$]	A[ν(free CO_2H)]/ A[ν(H-bonded CO_2H)]
	[MUA] = 3.0 μM	
	0.26	
15	0.16	0.31
30	0.13	0.17
120	0.15	0.27
	[MUA] = 0.4 μM	
	0.26	
5	0.21	1.02
15	0.20	1.05
45	0.20	1.23
90	0.20	1.11

methylene stretching modes (e.g., $\nu_{a\&s}(CH_3)$ and $\nu_{a\&s}(CH_2)$) in the high-frequency region.[15a]

In the high-frequency region (A), the increasing absorbance of methylene stretching bands at 2918 and 2848 cm^{-1} supports that the network structure is primarily composed of alkyl chains. The methyl stretching bands are small but detectable at 2960 and 2878 cm^{-1}. In comparison with the relative absorbance ratio of the methyl band (ν_a (CH_3)) vs the methylene band (ν_a (CH_2)), i.e., A($\nu_a(CH_3)$)/A($\nu_a(CH_2)$), for the cast DT-Au nanoparticles (d), a reduction is evident for the MUA-linked nanoparticle films, indicating a partial replacement of the capping DT by MUA molecules (see Figure 3 from a to b, and Table 1). The fact that there is little shift in both $\nu_a(CH_2)$ and $\nu_s(CH_2)$ bands as a function of immersion time is in contrast to those observed for self-assembled monolayers with a similar chain length,[23] where $\nu_a(CH_2)$ shifted from 2926 to 2918 cm^{-1} due to an increased packing of the alkyl chains. This observation demonstrates that the packing structure of the shell in the thin film assembly remains crystalline-like.[24−26] The relatively little change in the ratio **A**$\nu_a((CH_3))$/**A**($\nu_a(CH_2)$) (Table 1) after the initial layer formation indicates the structural similarity of the linked nanoparticles in the different growth layers.

In the low-frequency region (B), two overlapping bands diagnostic of carboxylic acid groups can be identified at 1710 and 1743 cm^{-1}. In our earlier study of MUA-linked 2∼5 nm nanoparticles from higher concentration solutions,[15a] the bands observed at 1740, 1710, and ∼1670 cm^{-1} were assigned to free, head-to-head hydrogen-bonded and polymeric hydrogen-bonded $-CO_2H$ groups, respectively. As shown by the spectral deconvolution (Figure 3B, insert, and Table 1), the polymeric H-bonding component is largely absent. The relative ratio of free (1740 cm^{-1}) vs hydrogen-bonded (1710 cm^{-1}) CO_2H groups, i.e., **A**[ν(free)]/**A**[ν(H-bonded)], is dependent on the immersion time. The relatively small change after the initial layer formation (b) indicates again the structural similarity in the subsequent hydrogen-bonding for the thin film growth. In general, the free-acid component is less than 20% of the total $-CO_2H$ groups, suggesting a predominant head-to-head hydrogen-bonding.

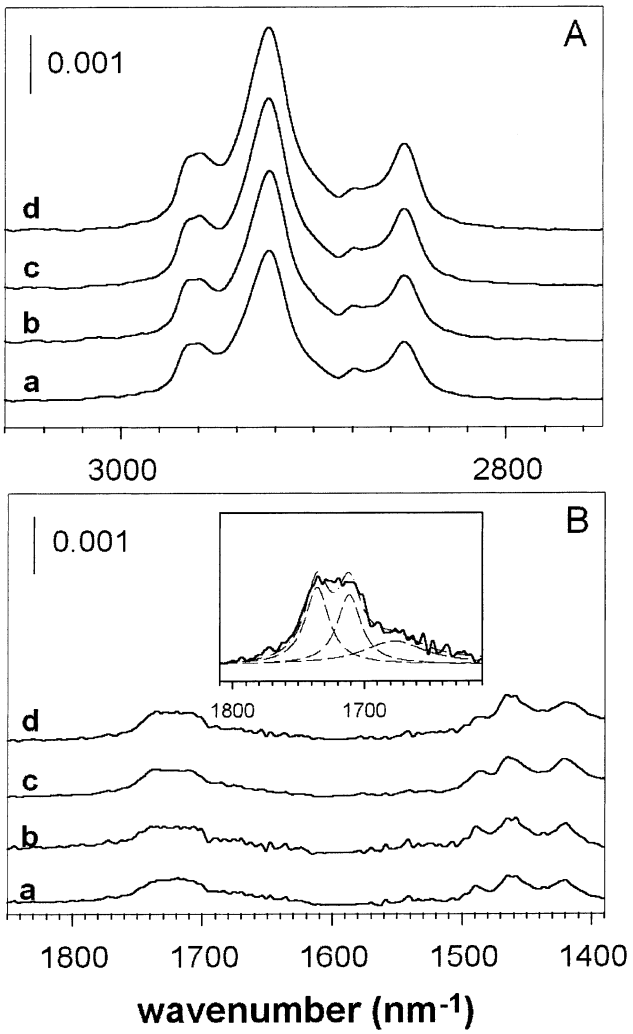

Figure 4. IRS spectra in high (A) and low (B) frequency regions for MUA-linked Au_{6-nm} films assembled from a hexane solution of [Au_{6-nm}] = 0.24 μM and [MUA] = 0.4 μM as a function of assembling time ($t_{assembly}$: 5 (a), 15 (b), 45 (c), and 90 (d) min). Insert: spectral deconvolution of the carbonyl-stretching envelope.

The spectral evolution was dependent on the concentration of MUA. Figure 4 shows another set of IRS spectra for thin films prepared at an 8-fold lower concentration of MUA (0.4 μM). The MUA-to-Au_{6-nm} molar ratio (1.6) was also reduced by a factor of ∼4. By comparing Figures 3 and 4, it is evident that while the C−H stretching region shows a very similar evolution, the carbonyl region reveals two major distinctions. First, the absorbance is much weaker for the low concentration case, suggesting a relatively smaller extent of exchange. The relatively little change in absorbance is again indicative of the structural similarity in layer-by-layer growth. Second, the spectral deconvolution (Figure 4B, insert, and Table 1) shows that the relative absorbance ratio of the hydrogen-bonded (1710 cm^{-1}) vs free (1740 cm^{-1}) $-CO_2H$ groups remains constant during the film growth, each of which is ∼40% of the total (in addition to a ∼20% of polymeric hydrogen-

(23) Bensebaa, F.; Voicu, R.; Huron, L.; Ellis, T. H.; Kruus, E. *Langmuir* **1997**, *13*, 5335.
(24) (a) Porter, M. D.; Bright, T. B.; Allara, D. L.; Chidsey, C. E. D. *J. Am. Chem. Soc.* **1987**, *109*, 3559. (b) Nuzzo, R. G.; Dubois, L. H.; Allara, D. L. *J. Am. Chem. Soc.* **1990**, *112*, 558. (c) Walczak, M. M.; Chung, C. K.; Stole, S. M.; Widrig, C. A.; Porter, M. D. *J. Am. Chem. Soc.* **1991**, *113*, 2370.
(25) Hostetler, M. J.; Stokes, J. J.; Murray, R. W. *Langmuir* **1996**, *12*, 3604.
(26) Maye, M. M.; Luo, J.; Han, L.; Zhong, C. J. *Nano Lett.* **2001**, *1*, 575.

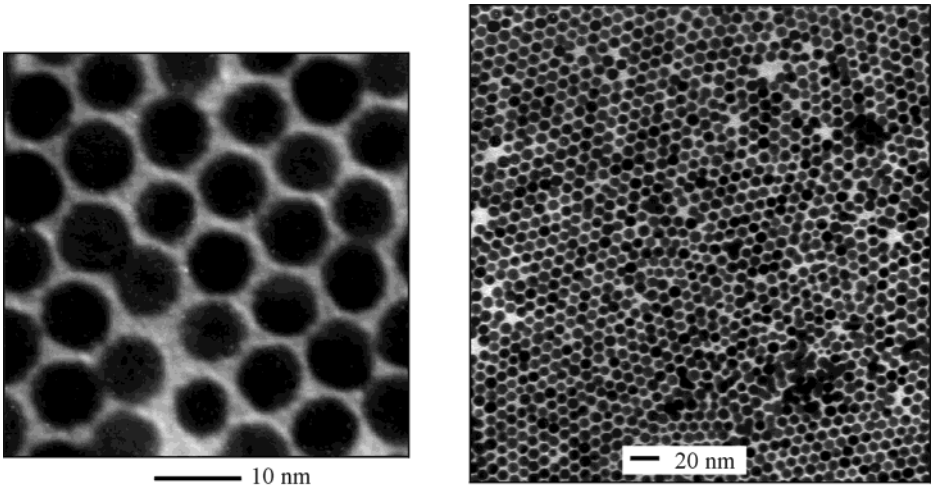

Figure 5. TEM micrographs of MUA-linked Au_{6-nm} assembly from a hexane solution of $[Au_{6-nm}] = 0.24\ \mu M$ and $[MUA] = 0.39\ \mu M$ ($t_{assembly}$: 12 min).

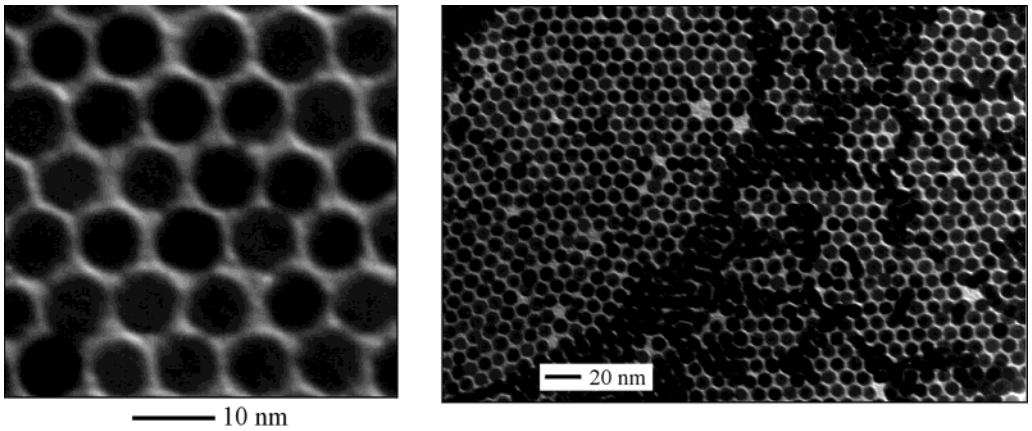

Figure 6. TEM micrographs of MHA-linked Au_{6-nm} assembly from a hexane solution of $[Au_{6-nm}] = 0.24\ \mu M$ and $[MHA] = 0.39\ \mu M$ ($t_{assembly}$: 15 min).

bonding component (~1640 cm^{-1})). The finding is in sharp contrast to the fact that less than 20% of free acid was observed for the films from a higher MUA concentration, indicating a relatively lower extent of hydrogen-bonding.

The dependence of the nanoparticle assembly on the concentration of MUA shows the effective mediation of the interparticle hydrogen-bonding. The MUA-to-nanoparticle molar ratio of ~1 translates to ~1 MUA per ~500 capping DT molecules on the nanocrystal (Au_{6-nm}) in the solution. As shown in Table 2 by the relative changes of the characteristic bands, the extent of exchange clearly decreases when the MUA concentration is decreased. These insights are important for assessing the interparticle morphological properties, as described next.

2. Interparticle Morphology. *A. Ordered Array.* Figure 5 shows a representative TEM micrograph for a thin film assembly prepared from a hexane solution of MUA (0.39 μM) and DT-capped Au_{6-nm} (0.24 μM). The preparation involved a vertical immersion of a carbon-film-coated TEM grid in the solution that was followed by an immediate thorough rinsing with hexane upon emersion. The assembly displays large domains of an ordered array with hexagonal packing. Such a morphology was not observed in a control experiment (i.e., the same preparative procedure and solution constituents but in the absence of MUA). A close comparison with DT/Au_{6-nm} nanoparticles evaporated on the TEM grid (Figure 1) reveals a subtle difference in packing density. It is important to emphasize that although the evaporated DT/Au_{6-nm} film can be redissolved in hexane, the MUA-linked film is not soluble in either hexane or ethanol solvent. The driving force for the interparticle packing in the DT/Au_{6-nm} case involves only VW interaction through interdigitation of alkyl chains.[15] For the MUA-linked film, a combination of hydrogen-bonding and VW interactions must be involved, as revealed by IRS data.

Similar features of the interparticle ordering have also been observed using a different chain length in the mediator structure, i.e., MHA, to assemble Au_{6-nm} particles (Figure 6). The assembly also displays large

Table 2. Dependence of the $A[\nu_a(CH_3)]/A[\nu_a(CH_2)]$ and $A[\nu_a(CH_2)]/A[\nu(CO_2H)]$ Ratios on the MUA Concentration in the Assembly of MUA-Linked Gold Nanoparticles

[MUA] (μM)[a]	$A[\nu_a(CH_3)]/A[\nu_a(CH_2)]$	$A[\nu_a(CH_2)]/A[\nu(CO_2H)]$
0	0.26	
0.4	0.20	3.6
3.0	0.15	2.8
50	0.01	2.2

[a] Corresponding to the MUA concentrations of 0.4, 3.0, and 50, the [MUA]-to-nanoparticle mole ratio is 1.7, 6.3, and 50, respectively.

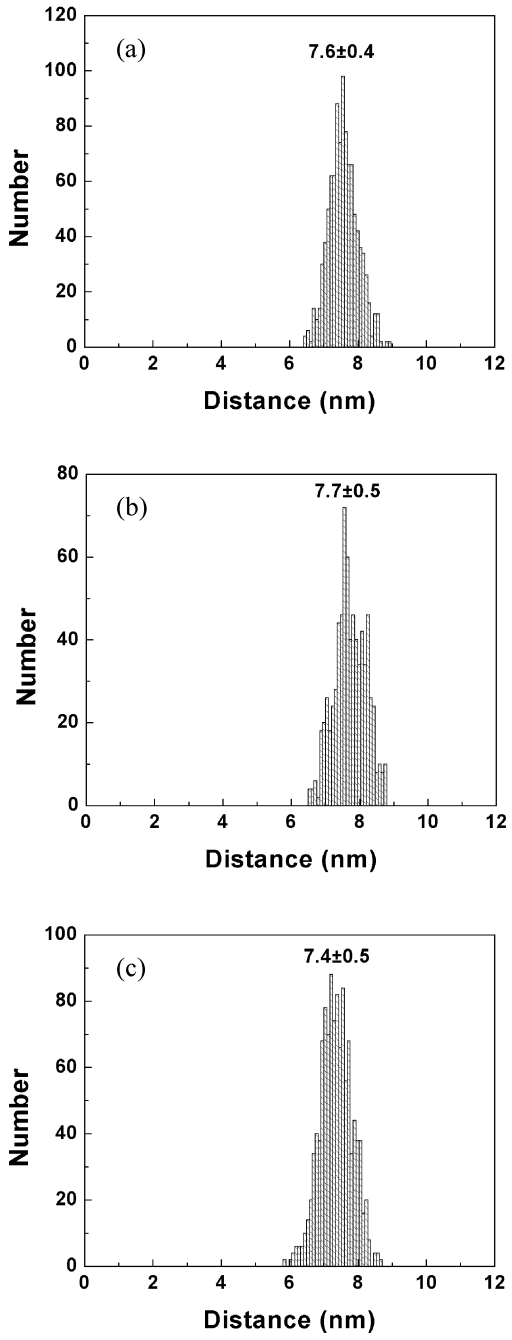

Figure 7. Statistical analysis results of the number of nanoparticles vs the interparticle center-to-center distances based on the TEM images in Figures 1a, 5b, and 6c.

domains of ordered array with hexagonal packing. The apparent two-layer patches or spots are either due to the formation of a second layer of nanoparticles on the first layer or nanoparticles assembled on the other side of the grid. Again, a comparison with the evaporated DT/Au_{6-nm} particles reveals subtle differences in the periodicity or interparticle spacing and in the solubility, similar to those for the MUA-linked nanoparticles.

To determine the interparticle distance in the above ordered arrays, a direct method is to measure the average center-to-center or edge-to-edge distances. As shown in Figure 7, we mapped the interparticle center-to-center distances via a software-assisted statistical analysis of the data in Figures 1, 5, and 6, from which the edge-to-edge distance was calculated by subtracting

Table 3. Average Interparticle Distances Derived from TEM Image Analyses of the Data in Figures 1, 5, and 6

	interparticle distance	
assembly	d_1 (center-to-center) (nm)[a]	d_2 (edge-to-edge) (nm)[b]
(a) DT−Au_{6-nm}	7.7 (±0.5)	1.5
(b) MUA-linked Au_{6-nm}	7.4 (±0.5)	1.2
(c) MHA-linked Au_{6-nm}	7.6 (±0.4)	1.4

[a] Based on a computer analysis of domains with 1300 counts of particles for a and 250 counts for b and c. [b] Based on d_1 and a spherical model for the particle (average diameter: 6.2 ± 0.5 nm).

the average diameter of the nanoparticles. Table 3 summarizes the results. Because the edge-to-edge distances were derived from the center-to-center distances, they should be within the same statistical uncertainty. The DT/Au_{6-nm} array formed by evaporation has an average edge-to-edge distance of 1.5 nm, which is quite consistent with the expectation based on a model of interdigitation of alkanethiolates on the shells between neighboring nanoparticles.[1,5,27] Interestingly, this value is slightly different from both MUA-linked Au_{6-nm} (1.2 nm) and MHA-linked Au_{6-nm} (1.4 nm). The edge-to-edge distance for the MHA-linked Au_{6-nm} assembly appears comparable to that for the MUA-linked Au_{6-nm} in view of the standard deviation. A key observation here is that the average edge-to-edge distance is much smaller than expectation based on a model of 100% head-to-head hydrogen-bonding between $-CO_2H$ terminal groups of the trans alkyl chain structure. The modeling analysis would yield ~3.6 nm for $(MUA)_2$ and ~4.8 nm for $(MHA)_2$.

To account for the interparticle distance being smaller than the expected lengths, we have considered several interparticle interaction forces. Two of the most important forces are VW and hydrogen-bonding interactions for the examined systems. The former occurs via interpenetration of the alkyl chains,[27] whereas the latter occurs at the terminal functional groups. We believe that a combination of the two interactions played a significant role in the final interparticle packing after the initial mediation by exchange and hydrogen-bonding. This assessment is supported by the shell composition. In comparison with the extent of exchange (~8% DT) for samples prepared at high N_L/N_{NP} ratios, the shell for thin films prepared at a very small N_L/N_{NP} molar ratio (1~2) must consist of a larger fraction of DT. This is evidenced by the IRS and solubility data. For the mixed $-CO_2H$ and $-CH_3$ shell, while the relatively limited sites of hydrogen-bonding mediate the interparticle linking, the inter-penetration of DT thiolate components has the propensity of maximizing the interdigitative cohesive interaction. The combination of the two forces leads to a "squeezed" interparticle spatial property (Scheme 2), which is neither purely VW interdigitation as known for cast alkanethiolate-capped nanoparticles,[5,27] nor purely interdigitated hydrogen-

(27) (a) Wang, Z. L.; Harfenist, S. A.; Whetten, R. L.; Bentley, J.; Evans, N. D. *J. Phys. Chem. B* **1998**, *102*, 3068. (b) Petroski, J. M.; Green, T. C.; El-Sayed, M. A. *J. Phys. Chem. A* **2001**, *105*, 5542.

(28) (a) Liu, J.; Shin, Y.; Nie, Z. M.; Chang, J. H.; Wang, L. Q.; Fryxell, G. E.; Samuels, W. D.; Exarhos, G. J. *J Phys. Chem. A* **2000**, *104*, 8328. (b) Li, L. S.; Jin, J.; Yu, S.; Zhao, Y. Y.; Zhang, C. X.; Li, T. J. *J. Phys. Chem. B* **1998**, *102*, 5648.

Scheme 2. "Squeezed" Packing Model Involving Hydrogen-Bonding at Carboxylic Acid Groups and Cohesive Interaction through Interdigitation of the Alkyl Chains

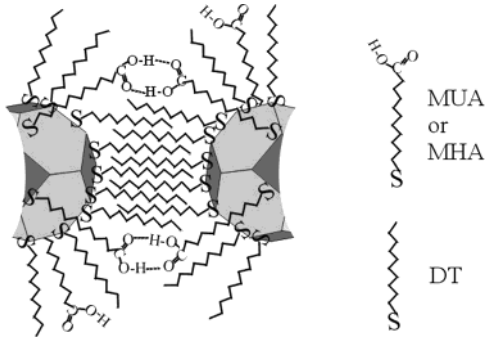

bonding as proposed for nanoparticles capped with amide-functionalized thiolates.[13] We note that smaller interparticle distances have been reported for gold or silver nanoparticle assemblies[1,5,20,27,31−33] that do not involve interparticle hydrogen-bonding interactions. The "squeezed" model proposed in this paper is also in agreement with a recent report by Zamborini et al.[32] that concluded a similar observation from electrical and optical measurements about the interparticle properties for a Cu^{2+}-carboxylate bridged gold nanoparticle assembly.

The evidence to support the "squeezed" interparticle spatial model has been provided by grazing angle X-ray diffraction characterization and a comparison with the nanoparticle assembly thickness data from two different techniques, AFM and QCM. The former provided a *d* spacing value of 5.1 nm for a MUA-linked Au_{5-nm} film deposited on glass substrate (see Supporting Information). This value is comparable to an estimate from the inter-layer distance of closely-packed nanoparticles on the substrate, and is largely consistent with the expectation based on the TEM result. The latter allowed the determination of the total mass of assembled nanoparticles from which the thickness can be derived based on the particle size and interparticle edge-to-edge distance. The 6.2-nm nanoparticle is modeled as a truncoctahedron,[4a] which gives 8307 gold atoms and 713 thiolates. Table 4 shows the data determined for a MUA-linked Au_{6-nm} film. The data for a NDT-linked Au_{6-nm} film are also included for comparison. The results reveal a very good agreement between the AFM-determined (8.0 nm) and the QCM-determined thickness (8.2 nm) when the edge-to-edge distance of 1.2 nm is used. The data therefore support the "squeezed" interparticle spatial model in Scheme 2. In the case of NDT interparticle linking, while only very small domains of ordered array (∼15 particles) could be identified, the estimated average edge-to-edge distance (1.4 nm) was only slightly smaller than the theoretical distance (1.5 nm). The close agreement between the AFM- (17.2 nm) and the QCM-determined thickness (20.1 nm) further supports the above assessment.

Table 4. Comparison of Thin Film Thickness Determined from Quartz-Crystal Microbalance (QCM) and AFM for the Mediator-Linked Gold Nanoparticle Films

	film thickness[a], *d* (nm)			
	by AFM	by QCM		
assembly	*d*	Δf (Hz)[b]	*d*[c]	*d*[d]
(a) MUA-linked Au_{5-nm} film	8.0 ± 0.3	2523 ± 10	19.0	8.2
(b) NDT-linked Au_{5-nm} film[e]	17.2 ± 0.4	5426 ± 10	20.9	20.1

[a] The nanoparticle films were assembled on a 10-MHz polished quartz crystal coated with a gold film. [b] Δf is translated to mass loading (Δm) based on Sauerbrey's equation $\Delta m = -C_f \Delta f$, where the mass sensitivity $C_{xc4} = 5.5$ ng/cm^2/Hz. [c] Calculated from Δf, using a theoretical edge-to-edge distance of 3.6 nm based on an idealized model of the head-to-head hydrogen-bonding by Au−$S(CH_2)_{10}CO_2H\cdots HO_2C(CH_2)_{10}S$−Au. [d] Calculated from Δf, using the experimental edge-to-edge distance of 1.2 nm, which is determined from the ordered array (Table 3) and is hypothesized as hydrogen-bonding mediated cohesive interparticle linkage (Scheme 2). [e] Based on very small domains (average domain size ∼15 particles) of ordered array in TEM micrograph for NDT−Au_{6-nm} film. The determined average edge-to-edge distance was 1.4 ± 0.5 nm.

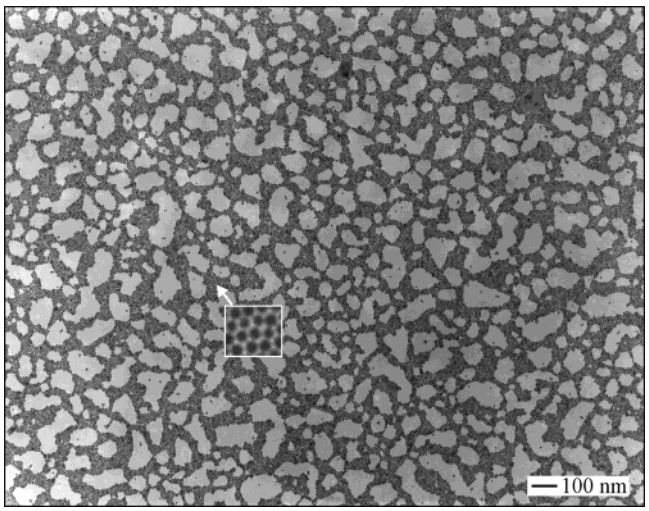

Figure 8. TEM micrograph of the branching morphology for a MUA-linked Au_{6-nm} film assembly from a hexane solution of [Au_{6-nm}] = 0.24 μM and [MUA] = 0.39 μM ($t_{assembly}$: 15 min). Insert: an enlarged view.

We also note that the interparticle ordering depends on size and monodispersity of the nanoparticle cores. Using 2∼5-nm core-sized particles which are relatively less monodispersed (≥0.6), we did not detect significant domains of ordered arrays (see Supporting Information). The capability of large and monodispersed nanoparticles to maximize the inter-shell cohesive interaction is consistent with a recent finding from a study of resorcinarene-encapsulated gold nanoparticles (16−170 nm),[12e] which showed that the interparticle distance decreases with core size and is much smaller than the expected size of the capping molecule.

B. 2D Branching. Figure 8 shows another representative TEM micrograph for a MUA-linked Au_{6-nm} thin film

(29) Fujii, T.; Yano, T.; Nakamura, K.; Miyawaki, O. *J. Membrane Sci.* **2001**, *187*, 171.
(30) (a) Gulley, G. L.; Martin, J. E. *J. Colloid Interface Sci.* **2001**, *241*, 340 (b) Hiddessen, A. L.; Rodgers, S. D.; Weitz, D. A.; Hammer, D. A. *Langmuir* **2000**, *16*, 9744. (c) Hanus, L. H.; Sooklal, K.; Murphy, C. J.; Ploehn, H. J. *Langmuir* **2000**, *16*, 2621. (d) de Hoog, E. H. A.; de Jong-van Steensel, L. I.; Snel, M. M. E.; van der Eerden, J. P. J. M.; Lekkerkerker, H. N. W. *Langmuir* **2001**, *17*, 5486.
(31) Motte, L.; Lacaze, E.; Maillard, M.; Pileni, M. P. *Langmuir* **2000**, *16*, 3803.
(32) Zamborini, F. P.; Leopold, M. C.; Hicks, J. F.; Kulesza, P. J.; Malik, M. A.; Murray, R. W. *J. Am. Chem. Soc.* **2002**, *124*, 8958.
(33) (a) Ohara, P. C.; Gelbart, W. M. *Langmuir* **1998**, *14*, 3418. (b) Ohara, P. C.; Heath, J. R.; Gelbart, W. M. *Angew. Chem., Int. Ed. Engl.* **1997**, *36*, 1078. (c) Maenosono, S.; Dushkin, C. D.; Saita, S.; Yamaguchi, Y. *Langmuir* **1985**, *1*, 5, 957.

prepared from a dilute solution, which is characteristic of 2D branching as depicted in Scheme 1(b). The film displays a clear nanoporous network created by the branched architecture with an average pore size of ~80 nm. A certain fraction of the nanoparticle array similar to the ordered arrays described in the previous subsection is evidently embedded in the 2D branching architecture. Under a given concentration, the relative coverage of the densely packed array area vs the 2D branched pore area is highly dependent on the monodispersity of the nanoparticles. By increasing monodispersity, the average size of the pore decreases. The 2D branching morphology is also dependent on the N_L/N_{NP} ratio. For example, pore sizes of an average diameter of 30−60 nm were observed using a much smaller MUA concentration (e.g., 0.4 μM). In contrast, much smaller pore sizes were observed when using a much larger ratio ($\geq$50). In the latter case, the particles were densely packed in a 3D architecture.

We have also observed similar branching or fractal growth phenomena on other substrates. For example, for a thin film assembled on a Au/mica substrate under a similar condition, domains of dense packing and branching morphology as large as a few microns have been observed using AFM (see Supporting Information). Although not as well resolved as in the TEM image due to tip−sample convolution of the AFM imaging, a close examination can identify subtle branching morphology. The cross-section view reveals a height variation corresponding to the size of the assembled nanoparticles.

To a certain degree, the branched structure resembles those of fractal aggregation for colloids[28] known in sol−gel technology. The fractal growth can be described by mass fractal dimension (d),[29] i.e., $M \propto R^d$, where M represents the mass of the branched structure and R is the corresponding radius. The fractal component d equals 2 for 2D growth on a planar substrate, and equals 3 for growth in 3D space. Importantly, on the basis of our earlier kinetic studies of the mass changes in the nanoparticle assembling process to which the fractal component can be related,[15b] we found an exponential growth which is characteristic of a reaction-limited aggregation process mediated by the linker molecules for the formation of both the compact and branching morphologies.[30] We also note that the lack of symmetry is partially responsible for the formation of the branched morphology in Figure 8. Under such a low concentration of linker molecules, it is possible that some of the exchanged $-CO_2H$ ligands are not symmetrically distributed in the shell. The mechanistic details are a subject of our further investigation.

Conclusions

In conclusion, we have demonstrated that the use of a highly dilute concentration of carboxylic acid functionalized alkanethiol mediation agent in the assembly of decanethiolate-capped gold nanoparticles leads to the formation of controllable interparticle packing, ordering and branching. A "squeezed" interparticle spatial model involving both hydrogen-bonding at the carboxylic acid terminal groups and cohesive VW interdigitation of the capping decanethiolate molecules is concluded to be responsible for the interparticle assembling forces. This model implies that the $-CO_2H$ groups are mostly located at the interparticle void spaces, which shines new light into the mechanistic aspect in our recent finding of ion-channeling properties of the nanostructured thin films.[15a] The interparticle morphologies can be controlled by manipulating an extremely small quantity of the carboxylic acid functionalized alkanethiol mediation agent. We further note that the use of simple alkanoic acid did not produce any of the phenomena reported in this paper, thus ruling out possible surfactant effects. These findings are significant because the controllable 2D morphology with a regulation in interparticle spatial properties may be exploited for manipulating mass transport in nanostructured sensor or catalysis applications where the interparticle distance is an important parameter. The two-component interparticle forces may be generalized to many nanoparticle assemblies involving different mediators including organic, inorganic, polymeric, and biological molecules such as vesicle aggregation with a controlled ligand−receptor stoichiometry.[34] A further study of the interfacial nanochemistry in terms of models of reaction- vs diffusion-limited assembling processes[30] as well as fractal dimension theory[29] is in progress.

Acknowledgment. We thank Mr. H. Eichelberger for assistance in TEM measurement. Financial support of this work from the Petroleum Research Fund administered by the American Chemical Society and the 3M Corporation is gratefully acknowledged.

Supporting Information Available: GXRD spectrum for a MUA-linked DT/Au_{5-nm} film on glass substrate, TEM images of the subject materials and a size-distribution plot, and an AFM image of the MUA-linked Au_{6-nm} film (PDF). This material is available free of charge via the Internet at http://pubs.acs.org.

CM0208051

(34) Kisak, E. T.; Kennedy, M. T.; Trommeshauser, D.; Zasadzinski, J. A. *Langmuir* **2000**, *16*, 2825.